Crystallographic account of nano-scaled intergrowth of M₂B-type borides in nickel-based superalloys

X.B. Hu, Y.L. Zhu, X.L. Ma *

Shenyang National Laboratory for Materials Science, Institute of Metal Research, Chinese Academy of Sciences, Shenyang 110016, People's Republic of China

Abstract

M₂B-type borides in nickel-based superalloys containing boron subjected to long-term aging treatments were investigated by means of analytical transmission electron microscopy. Contrast analysis and electron diffraction show that the boride precipitations have dual-phase structures ($I4/mcm$, C16; $Fddd$, C$_b$) with a high density of stacking faults. The faulted planes and displacement vectors are determined as $(110)_{C16}$ and $[1\bar{1}1]_{C16}/4$ in C16 structure and $(100)_{Cb}$ and $[011]_{Cb}/4$ in C$_b$ structure. Structural models based on a polyhedron of square anti-prisms are proposed not only to rationalize the stacking faults, 60° rotation twin and the intergrowth of structural variants, but also to interpret the newly observed structure in M₂B-type borides.

1. Introduction

On account of their excellent combination of properties at elevated temperatures, nickel-based superalloys play a key role in many crucial applications, such as the hottest parts of jet engines used in aircraft and various industrial gas turbines [1,2]. As an essential micro-alloying element, boron is extensively added to superalloys to strengthen the grain boundaries and improve the creep rupture properties [3–5]. Boron is usually present in the form of boride, such as M_3B_2, M_5B_3 and M_2B [6–11], where M denotes transitional metals. Among these borides, knowledge on M_2B is quite controversial. The M_2B phase has rarely been studied in Ni-based superalloys [9,11], although it was relatively widely documented in steels [12–15].

M₂B-type boride has a dual-phase characteristic. One of its structural variants has a body-centered tetragonal structure (*Strukturbericht* notation C16, space group $I4/mcm$) and another has face-centered orthorhombic structure (*Strukturbericht* notation C$_b$, space group $Fddd$). Nevertheless, some microstructural issues remain unclarified. First, in an earlier study, Goldfarb et al. [13] proposed that C16 and C$_b$ structures intergrow with the orientation relationship $[001]_{C16}//[001]_{Cb}$ and $(1\bar{1}0)_{C16}//(100)_{Cb}$. In contrast, according to a recent study by Zhang and Ojo [9], the orientation relationships between these two variants are labeled as $[1\bar{1}1]_{C16}//[001]_{Cb}$ and $(110)_{C16}//(100)_{Cb}$. Second, although stacking faults were frequently reported in both C16 and C$_b$ M₂B-type borides [9,11,13], the displacement vector, which is a key parameter describing the stacking fault, has not been determined so far. Third, in the proposal of structural variants of M₂B-type borides derived from the lattice fringe images [13], translational periodicity and structural details in each sub-layer were not taken into account.

So far, the crystallography of M₂B-type borides remains debatable, which is believed to result from the fact that

they always contain a high density of faults. Moreover, some of the electron diffraction patterns (EDP) in C16 are quite similar to those in C_b, which makes it difficult to identify the true lattice type of M_2B phase. In addition, the C_b is a pseudo-hexagonal structure, and hence some of its EDP can be indexed based on the hexagonal lattice [11]. Rotation twins in C_b-M_2B were also proposed [16], although detailed experimental investigations have not been carried out.

A thorough understanding of the crystallographic characteristics in M_2B-type borides is of great importance in setting up the relationships between properties and microstructures. The present work applies transmission electron microscopy (TEM) and extensively investigates the structural and defect properties of M_2B-type boride precipitation in a nickel-based superalloy. The present authors propose a polyhedron of square anti-prisms and rationalize the microstructural characteristics in M_2B-type borides.

2. Experimental procedures

The nominal composition of the Ni-based superalloys used in the present work is 15.5Cr, 10.8Co, 2.1Mo, 5.6W, 3.2Al, 4.6Ti, 0.2Nb, 0.4Hf, 0.073C, 0.075B and balance Ni, in wt.%. The as-cast alloys were subjected to solution treatment at 1170 °C for 4 h, followed by air-cooling. Subsequently, two-step aging treatments were applied. The primary precipitate aging treatment was performed at 1050 °C for 4 h and followed by air-cooling. The secondary aging treatment was carried out at 850 °C for 16 h and followed by air-cooling. Finally, the standard heat-treated alloys were exposed at 900 °C for 10,000 h and then air-cooled. TEM specimens were prepared by cutting, grinding, punching and dimpling to 10 μm. The ion-milling was carried out in a Gatan precision ion polishing system with a liquid-nitrogen-cooled stage to avoid preferential thinning effects. A Fischione plasma cleaner was used before acquiring composition analysis for preventing surface contamination.

Structural investigations were performed in a Tecnai G^2 F30 transmission electron microscope, equipped with a high-angle annular dark-field (HAADF) detector, X-ray energy-dispersive spectrometer (EDS) systems and Gatan imaging filter system, operated at 300 kV. The point resolution in the HRTEM mode is ~0.2 nm. Electron energy loss spectroscopy (EELS) spectra were collected with 0.3 eV per channel dispersion. The energy filtered TEM (EFTEM) images were recorded by the three-window method, and the slit width used here is 20 eV. The average background subtraction filter and Wiener filters were used to subtract the signal in HRTEM images arising from the amorphous layer at the surface of the specimen [17]. The Fast Fourier Transform pattern of the HRTEM image was used to determine the exact projected direction.

3. Results and discussion

3.1. Structural observation at a micrometer scale

After long aging treatment of the nickel-based superalloys bearing boron, M_2B-type boride precipitations are embedded in the matrix (γ/γ'). Fig. 1 is a bright-field TEM image showing the typical morphology of M_2B-type borides at the grain interiors. It is seen that these M_2B-type borides are partly or completely heavily faulted as indicated by I and II in Fig. 1.

3.1.1. Structure of M_2B-type boride

Owing to the tilting angle limitation of the TEM, the series EDP of a specific structural variant (either C16 or C_b) were acquired from more than one grain that is relatively perfect, with very few stacking faults. By doing so, all the low-indices EDP were collected and used for lattice construction. Moreover, at least two EDP were acquired in each grain in order to uniquely determine whether the structure of the grain was C16 or C_b. The EDP from the same variant were displayed together, as shown in Figs. 2 and 3, respectively. Lattice type and space group were derived based on the extinction rules in each variant, labeled in Tables 1 and 2, respectively. One of these structural variants has a body-centered tetragonal structure with space group $I4/mcm$ with lattice parameters $a = 0.52$ nm and $c = 0.43$ nm. That is to say, it is a C16-type M_2B. According to EDP in Fig. 3 and extinctions shown in Table 2, another structural variant is determined to have a face-centered orthorhombic structure with space group $Fddd$ and lattice parameters $a = 1.47$ nm, $b = 0.74$ nm and $c = 0.43$ nm, namely the C_b-type M_2B.

Fig. 1. Bright-field TEM image showing the precipitations of M_2B-type boride within the matrix (γ/γ'). Note that the precipitations feature highly dense stacking faults.
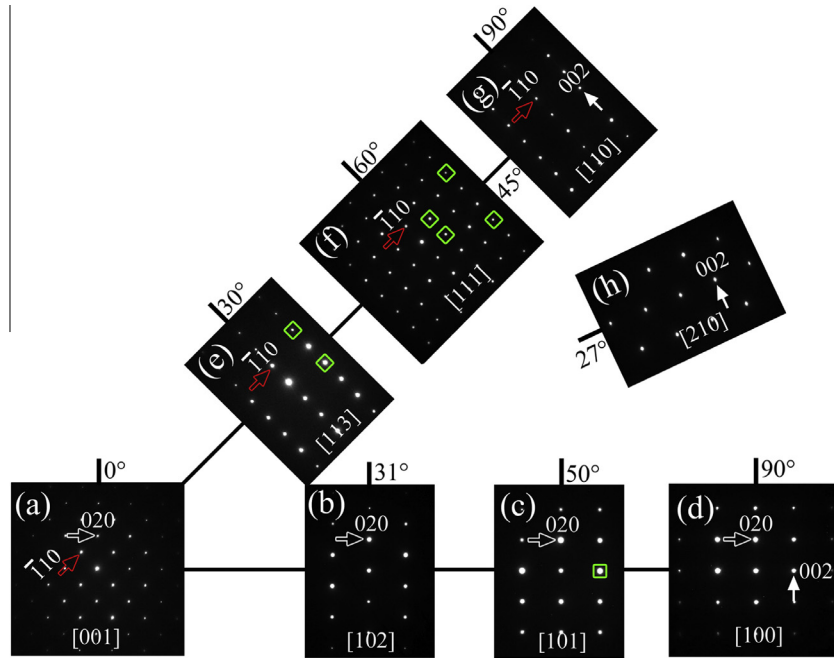
Fig. 2. A series of EDP of a M_2B-type boride obtained by large-angle tilting the crystal: (a) [001]; (b) [102]; (c) [101]; (d) [100]; (e) [113]; (f) [111]; (g) [110]; (h) [210] zone axis EDP. A C16-type M_2B with the space group $I4/mcm$ is determined according to the EDP. The square-framed diffraction spots are proposed to result from double diffraction.
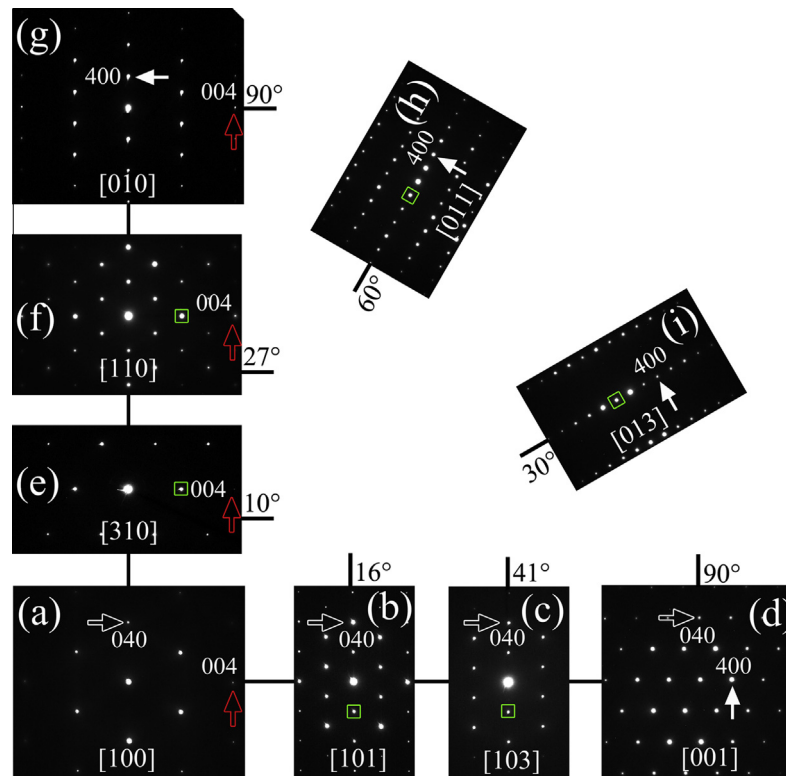

Fig. 3. A series of EDPs of a M_2B-type boride obtained by large-angle tilting the crystal: (a) [100]; (b) [101]; (c) [103]; (d) [001]; (e) [310]; (f) [110]; (g) [010]; (h) [011]; (i) [013] zone axis EDP. A C_b-type M_2B with the space group of $Fddd$ is determined according to the EDP.

3.1.2. Chemical composition of M_2B-type boride

Micro-analysis was performed in the STEM mode to display composition information. Fig. 4a is a HAADF image of a lath-shaped M_2B grain ~500 nm wide and several micrometers long. The matrix including γ and γ' and the M_2B-type boride precipitates are marked. Compared

Table 1
Reflection conditions of the body-centered tetragonal M_2B.

$(h00)$	$(0k0)$	$(00l)$	$(hk0)$	$(0kl)$	$(h0l)$	(hkl)
$h = 2n$	$k = 2n$	$l = 2n$	$h + k = 2n$	$l = 2n$	$l = 2n$	$h + k + l = 2n$

Table 2
Reflection conditions of the face-centered orthorhombic M_2B.

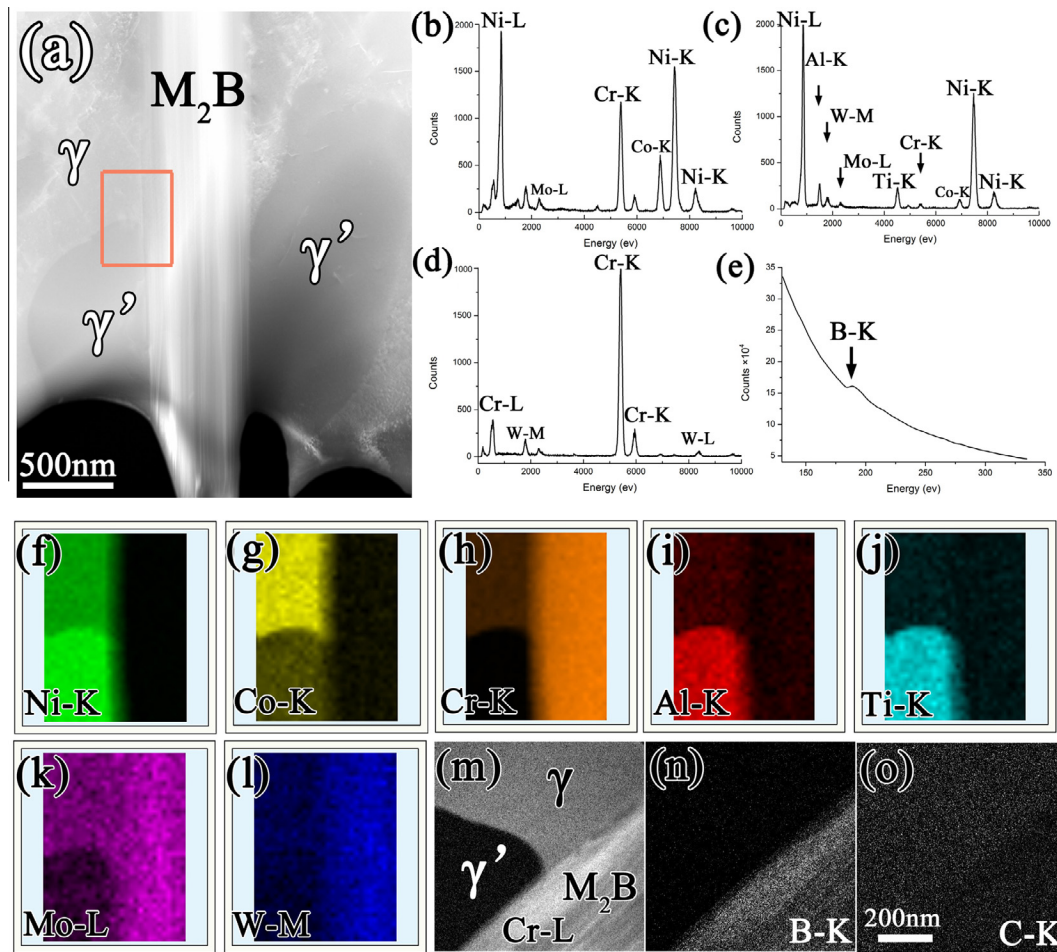| $(h00)$	$(0k0)$	$(00l)$	$(0kl)$	$(h0l)$	$(hk0)$	(hkl)
$h = 4n$	$k = 4n$	$l = 4n$	$k + l = 4n$	$h + l = 4n$	$h + k = 4n$	$h + k = 2n, h + l = 2n$
			$k, l = 2n$	$h, l = 2n$	$h, k = 2n$	$k + l = 2n$

Fig. 4. (a) HAADF image showing a typical morphology of lath-like M_2B-type boride precipitated at grain interior. (b)–(d) STEM–EDS spectra displaying the element distribution in γ, γ' and M_2B respectively. (e) TEM–EELS spectra acquired from the M_2B phase revealing the absorption edges of B–K at 188 eV. The peaks are indicated by arrows. (f)–(l) Element distribution map of Ni–K, Co–K, Cr–K, Al–K, Ti–K, Mo–L and W–M corresponds to the rectangle area shown in (a). (m)–(o) Energy filtered TEM images corresponding to Cr–L map, B–K map and C–K map, respectively.

with the matrix (γ and γ'), the M_2B phase shows brighter contrast under the HAADF imaging mode, owing to the relatively higher average atomic number (Z). According to the EDX results shown in Fig. 4b–d, the γ phase is composed of Ni, Cr, Co and a small amount of Mo, W; the γ' phase is composed of Ni, Ti, Al and a small amount of Cr, Mo, W; the M_2B phase is composed of Cr and a small amount of W and Mo. The boron–K edge peak for the M_2B boride is given in the EELS spectrum

shown in Fig. 4e. Moreover, compared with the γ phase, the γ' phase is rich in Ni, Ti, Al and lacks Co, Cr, Mo. Element W is distributed evenly in the γ and γ'. Similarly, compared with the matrix (γ and γ'), the M_2B precipitates are abundant in Cr, W. To detect the light element distribution such as carbon and boron, EFTEM was performed as shown in Fig. 4m–o. The EFTEM images are recorded from approximately the same area as the framed area shown in Fig. 4a.

3.1.3. 60° Rotation twin in C16-M$_2$B structure

Fig. 5a is a dark-field image (obtained using a coincident reflection from area I and II) showing a regular blocky M$_2$B grain within the matrix. The M$_2$B grain contains two areas, denoted by I and II. Fig. 5b–d shows EDP obtained from area I, while Fig. 5e–g shows EDP obtained simultaneously from area II. All the EDP can be indexed as C16-type M$_2$B structure. It is noted that all the diffraction patterns in Fig. 5b–g contain the $(110)_{C16}$ plane. In other words, about $[110]_{C16}$ rotation, the tilting of area I from $[001]_{C16}$ to $[1\bar{1}1]_{C16}$ corresponds to a tilting of area II from $[1\bar{1}1]_{C16}$ to $[1\bar{1}\bar{1}]_{C16}$. Fig. 5h is a schematic illustration showing the crystallographic relationships between these zone axes. Since the angles between $[001]_{C16}$ and $[1\bar{1}1]_{C16}$, $[1\bar{1}3]_{C16}$ and $[1\bar{1}0]_{C16}$, $[1\bar{1}1]_{C16}$ and $[1\bar{1}\bar{1}]_{C16}$ in C16 structure are all nearly 60°, areas I and II can be regarded as a 60° rotation twin with the rotation axis along the $[110]_{C16}$ direction. The orientation parallelism between C16 (area I) and its twin form C16-T (area II) can be deduced as

$$[002]_{C16}//[1\bar{1}1]_{C16\text{-}T}, [2\bar{2}0]_{C16}//[1\bar{1}3]_{C16\text{-}T} \text{ and } [110]_{C16}//[110]_{C16\text{-}T}$$

Stacking faults in $(110)_{C16}$ are of high density, according to the streaking lines seen in EDP (Fig. 5f).

3.2. Crystallographic considerations of C16 and C$_b$ structure

The polyhedron stacking model has been extensively applied to simplify the structure of topologically close-packed phases [18,19], M$_7$C$_3$-type carbide [20–22] and the TiB system [23,24]. Although the space groups of C16 and C$_b$ structures are different, they share the same building block: the square anti-prism consisting of one boron atom in the center and eight metal atoms in the vertex. By introducing the concept of polyhedron stacking in M$_2$B-type borides, it is found that the structural analysis can be greatly simplified.

Fig. 6a shows the unit cell of C16 structure with the square anti-prism indicated by the shadow areas. Fig. 6b is the projected image viewed along the $[001]_{C16}$ direction, displaying the fourfold symmetrical axis of C16 structure.

It is seen that the square anti-prisms share square faces with neighboring polyhedra along the $[001]_{C16}$ direction, while they share edges with neighboring polyhedra along the $\langle 110 \rangle_{C16}$ direction. For the C$_b$ structure, the unit cell with square anti-prisms indicated by shadow areas is shown in Fig. 6c. The neighboring polyhedra can be divided into two groups, colored yellow and green, respectively. Fig. 6d and e are projected images along the $[011]_{C_b}$ and $[01\bar{1}]_{C_b}$ direction, respectively. It is seen that the polyhedra in each group share faces with surrounding square anti-prisms along the $\langle 011 \rangle_{C_b}$ directions, while they share edges with neighboring square anti-prisms along the $\langle 01\bar{3} \rangle_{C_b}$ directions. The neighboring polyhedra in the different groups share edges.

Considering the same lattice parameter of the c axis in both C16 and C$_b$, it is believed that the above two structures may have a high degree of similarity along the $[001]$ direction. Fig. 7a shows the projection of C16 structure along the $[001]_{C16}$ direction. A basic structural unit A formed by 6 Cr atoms is defined as illustrated on the left-hand side of Fig. 7a. Then structural unit $\underline{A}$ could be obtained by the $c/2$ displacement of structural unit A. The characteristic projected length for the structural unit is also indicated in Fig. 7a. As mentioned earlier, the basic building block is the square anti-prism, and thus the simplified structure can be described by the large metal atoms. The boron atoms will be in particular sites for maintaining the basic building block once the locations of metal atoms are specified. Fig. 7b shows the stacking sequence of the derived structural units of A and $\underline{A}$ for the C16 structure viewed along the $[001]_{C16}$ direction. Similarly, to simplify the description of C$_b$ structure projected along the $[001]_{C_b}$ direction, another two structural units of B and $\underline{B}$ are denoted in Fig. 7c, which could be obtained by the $c/4$ and $3c/4$ displacements of structural unit A, respectively. The relative displacement between B and $\underline{B}$ is $c/2$. Fig. 7d is the projection of C$_b$ structure along $[001]_{C_b}$ illustrated by the structural units of A, $\underline{A}$, B and $\underline{B}$. It is seen that the C16 and C$_b$ structures have similar atom arrangements along the $[001]$ direction. And the $[220]_{C16}$, $[1\bar{1}0]_{C16}$, $[001]_{C16}$ directions of C16 structure should be
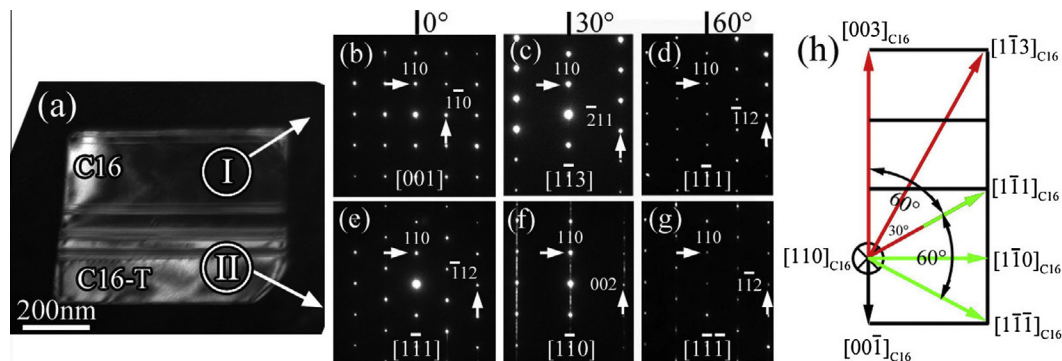

Fig. 5. (a) Dark-field image showing a 60° rotation twin within a M$_2$B grain. (b)–(d) EDP patterns taken from area I and indexed as $[001]_{C16}$, $[1\bar{1}3]_{C16}$ and $[1\bar{1}1]_{C16}$ zone-axis, respectively. (e)–(g) EDP obtained from area II with the same tilting condition as (b)–(d) corresponds to $[1\bar{1}1]_{C16}$, $[1\bar{1}0]_{C16}$ and $[1\bar{1}\bar{1}]_{C16}$ zone-axis, respectively. (h) Schematic illustration showing the crystallographic relationship of various orientations viewed along $[110]_{C16}$.
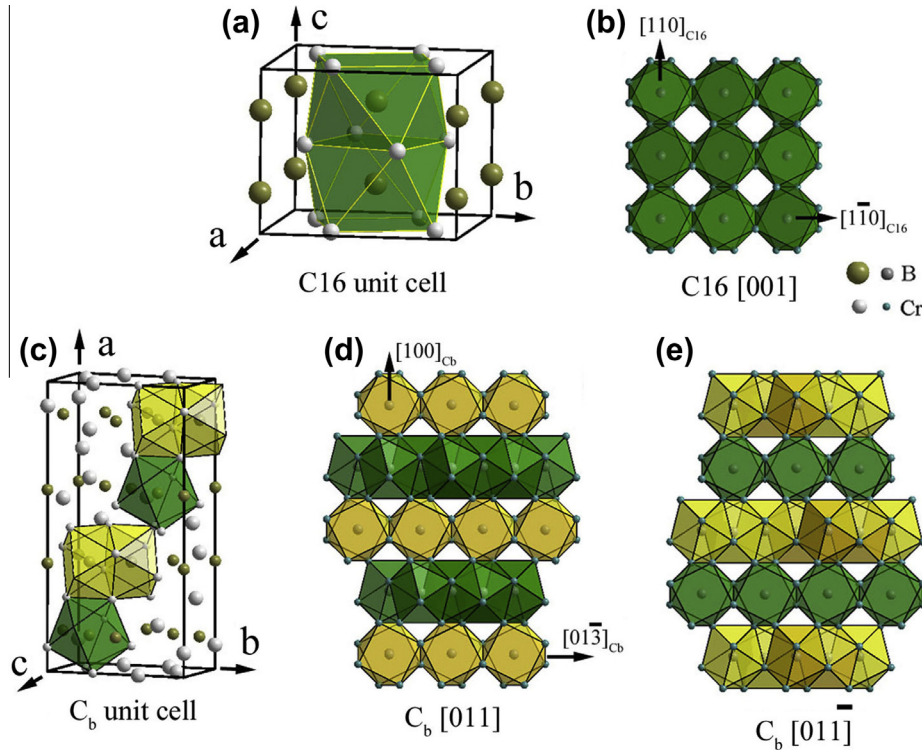
Fig. 6. (a) Atomic configuration of C16 structure in which square anti-prisms are shadowed. (b) Atomic projection along $[001]_{C16}$ showing the stacking sequence of square anti-prisms. (c) Atomic configuration of C_b structure in which square anti-prisms are shadowed. (d) and (e) Atomic projections from $[011]_{Cb}$ and $[01\bar{1}]_{Cb}$ directions of C_b structure, respectively. Note that the fourfold axis of the polyhedra is along the $[001]_{C16}$ direction in C16 structure, while the fourfold axis is along $[011]_{Cb}$ and $[01\bar{1}]_{Cb}$ in C_b.
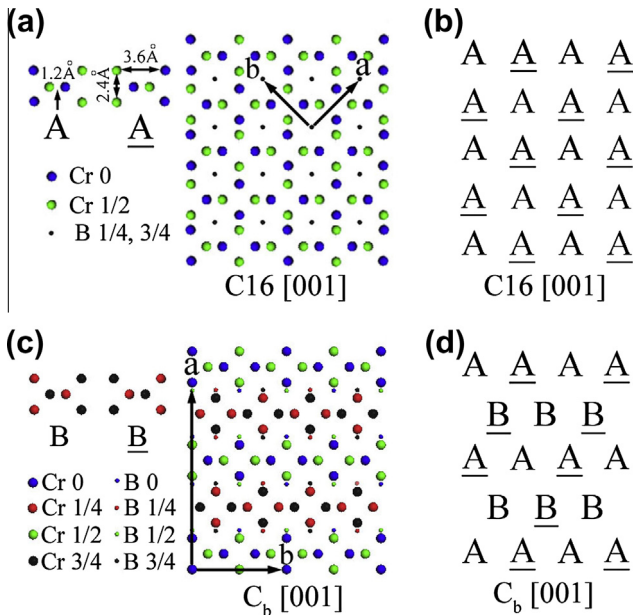

Fig. 7. (a) Atomic projection from $[001]_{C16}$ of C16 and (b) the corresponding simplified description. (c) Atomic projection from $[001]_{Cb}$ of C_b and (d) the corresponding simplified description. The unit cell vectors, atomic fractional coordinates and the characteristic projected lengths for the structure units (A, $\underline{A}$, B and $\underline{B}$) are indicated.

equivalent to the $[100]_{Cb}$, $[010]_{Cb}$, $[001]_{Cb}$ directions of C_b structure, respectively.

3.2.1. 60° Rotation twin for C16 and C_b structure

Based on the experimental information on the 60° rotation twins in the C16 structure, as displayed in Fig. 5, the $[1\bar{1}1]_{C16}$ direction should be equivalent to $[001]_{C16}$ in the C16 structure. Therefore, the atom arrangements along the $[1\bar{1}1]_{C16}$ and $[001]_{C16}$ directions must have a close relationship. To compare with the projected and simplified images along $[001]_{C16}$, as given in Fig. 7a and b, a projection of the C16 structure was made along the $[1\bar{1}1]_{C16}$ direction and, thereafter, a simplified form was displayed. First, it is of interest to note that the lattice length of the $[1\bar{1}1]_{C16}$ direction is twice that of the $[001]_{C16}$ direction (see Fig. 5h) and $[1\bar{1}1]_{C16}/2$ is a translation vector for the C16 structure. Then, a super cell can be defined with the basic vectors of $X = [110]_{C16}$, $Y = [1\bar{1}3]_{C16}$ and $Z = [1\bar{1}1]_{C16}/2$. After projecting the super cell along the Z direction with different Z fractional coordinates denoted by different colors, the typical characteristic for the projection can be revealed, as shown in Fig. 8a. Considering structural units (A, $\underline{A}$, B and $\underline{B}$) introduced in Fig. 7, the projection can be simplified as shown in Fig. 8b. Here structure units $\underline{A}$, B and $\underline{B}$ are obtained by a displacement of $[1\bar{1}1]_{C16}/4$, $[1\bar{1}1]_{C16}/8$ and $3[1\bar{1}1]_{C16}/8$ from unit A. Comparing Figs. 7a, b and 8a, b, it is clearly seen that the formation of the 60° rotation twin in the C16 structure is strongly correlated to the atom arrangements along the $[001]_{C16}$ and $[1\bar{1}1]_{C16}$ directions.
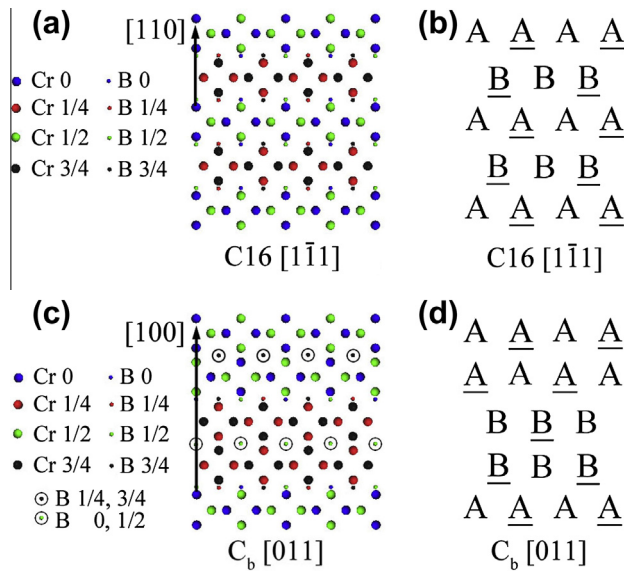
Fig. 8. (a) Atomic projections along $[1\bar{1}1]_{C16}$ of C16. (b) Simplified descriptions showing the stacking sequence of structural units in C16 along $[1\bar{1}1]_{C16}$ of C16. (c) Atomic projections along $[011]_{Cb}$ of C_b. (d) Simplified descriptions showing the stacking sequence of structural units in C_b along $[011]_{Cb}$ of C_b. Note that the atom fraction coordinates along the projected directions given here are based on $[1\bar{1}1]_{C16}/2$ for C16 structure and $[011]_{Cb}/2$ for C_b structure.

In addition, it is necessary to point out that the structure projections from both $[001]_{Cb}$ (Fig. 7c and d) and $[1\bar{1}1]_{C16}$ (Fig. 8a and b) directions are very similar and cannot be distinguished in the HRTEM mode, owing to the lack of height information along the projected directions.

Considering the fact that the C16 and C_b structures are constructed by the same building blocks of square anti-prism and the related directional equivalence between C16 and C_b, it is reasonable to suppose that the 60° rotation twin may exist in the C_b structure, as proposed by Mansfield [16]. Meanwhile, the $[011]_{Cb}$ direction for C_b structure is equivalent to the $[1\bar{1}1]_{C16}$ direction for the C16 structure. Therefore, the $[001]_{Cb}$ and $[011]_{Cb}$ directions in the C_b structure should have an equivalence too. Similarly, to compare the projected and simplified images along $[001]_{Cb}$, as given in Fig. 7c and d, a projection of the C_b structure was made along the $[011]_{Cb}$ direction, and then the related simplified form was exhibited. In the C_b structure, the lattice length of the $[011]_{Cb}$ direction is twice that of the $[001]_{Cb}$ direction, and $[011]_{Cb}/2$ is also a translation vector for the C_b structure. Again, a super cell can be defined as $X' = [100]_{Cb}$, $Y' = [01\bar{3}]_{Cb}$ and $Z' = [011]_{Cb}/2$ to reveal the projection characteristic along the Z' direction (see Fig. 8c). Based on the structural units (A, $\underline{A}$, B and $\underline{B}$) introduced in Fig. 7, the simplified form of Fig. 8c is shown in Fig. 8d. Structure units $\underline{A}$, B and $\underline{B}$ here are obtained by the displacement of $[011]_{Cb}/4$, $[011]_{Cb}/8$ and $3[011]_{Cb}/8$ from unit A, respectively. Furthermore, by comparison of Figs. 7c, d and 8c, d, it is speculated that the closely related atom arrangements along the $[001]_{Cb}$ and $[011]_{Cb}$ directions should result in a 60° rotation twin

in the C_b structure, which is further confirmed by the atomic scale observations.

On the basis of the crystallographic considerations for C_b structure in Figs. 7c, d and 8c, d, the orientation relationship between C_b and its twin form (namely, C_b-T) should be deduced as

$$[002]_{Cb}//[011]_{Cb-T}, [020]_{Cb}//[01\bar{3}]_{Cb-T} \text{ and } [100]_{Cb}//[100]_{Cb-T}$$

3.2.2. Intergrowth of C16 and C_b structure

On account of the stacking of structural units (A, $\underline{A}$, B and $\underline{B}$) for C16 and C_b structures along the $[001]$ direction shown in Fig. 7a–d, it is seen that C16 and C_b structures are closely related. The crystallographic orientation relationships for the basic intergrowth mode can be written as

$$[220]_{C16}//[100]_{Cb}, [1\bar{1}0]_{C16}//[010]_{Cb} \text{ and } [001]_{C16}//[001]_{Cb}$$

Meanwhile, considering the rotation twin in the C_b structure, the C16 structure can also grow with the twin form of C_b, namely, the twin-related intergrowth, which possesses the following orientation relationships

$$[002]_{C16}//[011]_{Cb}, [2\bar{2}0]_{C16}//[01\bar{3}]_{Cb} \text{ and } [220]_{C16}//[100]_{Cb}$$

or

$$[1\bar{1}1]_{C16}//[002]_{Cb}, [1\bar{1}\bar{3}]_{C16}//[020]_{Cb} \text{ and } [220]_{C16}//[100]_{Cb}$$

Now, it is clear that the disagreement between Ojo's experiment [9] and Goldfarb's model [13] for the orientation relationship of C16 and C_b actually results from the 60° rotation twin in C16 or C_b structure: the $[001]_{C16}//[001]_{Cb}$ relationship given by Goldfarb [13] is based on an normal intergrowth mode, while the $[111]_{C16}//[001]_{Cb}$ in Ojo's work on a twin-related intergrowth mode.

3.2.3. Stacking fault in C16 and C_b structure

It is interesting to note that the rotation twin does not destroy the basic anti-square prism building blocks for both C16 and C_b structures. Therefore, according to the stacking sequence of the structure units (A, $\underline{A}$, B and $\underline{B}$) along the $[001]_{C16}$, $[1\bar{1}1]_{C16}$, $[001]_{Cb}$ and $[011]_{Cb}$ directions shown in Figs. 7 and 8, stacking faults can be introduced into C16 and C_b structures with the polyhedron conserved. The faulted structure is projected along the $[001]_{C16}$ and $[001]_{Cb}$ directions and displayed in Fig. 9a and c, respectively. Again, the corresponding simplified descriptions with the structure units are given in Fig. 9b and d. Considering the inherent relationships between these structural units, the stacking fault planes and displacement vectors can be determined as $(110)_{C16}$ and $[1\bar{1}1]_{C16}/4$ for C16 structure, $(100)_{Cb}$ and $[011]_{Cb}/4$ for C_b structure. It is worth mentioning that a new ordered structure (referred as N1) is derived from the faulted C_b structure, which is indicated by vertical double arrows. The N1 structure is discussed in more detail in the following section.
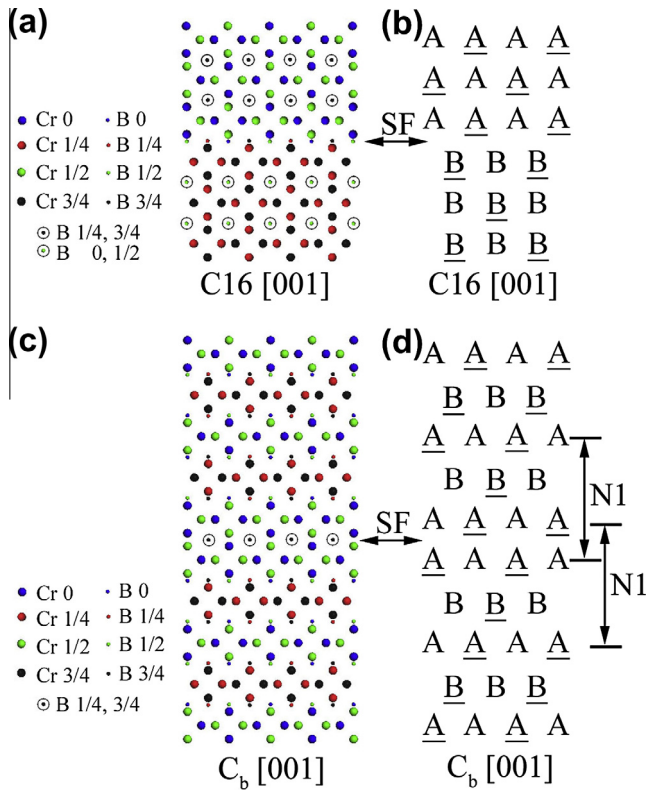
Fig. 9. Structure projection (a) and the corresponding simplified description (b) for C16 structure along the $[001]_{C16}$ direction with single stacking fault included; Structure projection (c) and the corresponding simplified description (d) for C_b structure along the $[001]_{Cb}$ direction with single stacking fault included. It is shown that a new order structure (referred as N1) as indicated by vertical arrows forms in the faulted C_b structure. The stacking faulted layers are indicated by horizontal arrows.

3.2.4. Polytypism in M₂B-type boride

Both C16 and C_b structures possess the basic polyhedron of square anti-prism, but their stacking modes are different. The C16 structure has only one set of square anti-prisms stacking along the $[110]_{C16}$ direction, and the fourfold axis of square anti-prisms is along the $[001]_{C16}$ direction, as shown in Fig. 6a and b. In contrast, in the C_b structure, the stacking of polyhedra is along the $[100]_{Cb}$ direction, and the fourfold axis of half the polyhedra is along the $[011]_{Cb}$ direction, whereas the other half are along the $[01\bar{1}]_{Cb}$ direction, as shown in Fig. 6d and e, respectively. Moreover, the $[001]_{Cb}$ direction is equivalent to the the $[001]_{C16}$ direction. Therefore, one could speculate a new basic structure (referred as N1), which has three sets of square anti-prisms with the fourfold axis of square anti-prisms along the $[001]_{Cb}$, $[011]_{Cb}$ and $[01\bar{1}]_{Cb}$ directions of C_b, respectively. Meanwhile, the basic lattice vectors of N1 structure written in an orthorhombic lattice form have a close relationship with those of C_b structure, namely, $\mathbf{a_{N1}} = 3\mathbf{a_{Cb}}/4$, $\mathbf{b_{N1}} = \mathbf{b_{Cb}}$ and $\mathbf{c_{N1}} = \mathbf{c_{Cb}}$. And the space group for the N1 structure is actually $P6_222$ (Ca in *Strukturbericht* notation) with $a = 0.43$ nm and $c = 1.10$ nm. Fig. 10a shows the $[001]_{N1}$ projection of N1 structure indicated in the orthorhombic lattice form.

In terms of the structural unit of A, $\underline{A}$, B and $\underline{B}$ defined for C16 and C_b structure in Fig. 7, the simplified form of N1 along the $[001]_{N1}$ direction is displayed in Fig. 10b.

Similarly, based on the directional equivalence in C16 and C_b structure, the C16 structure can also be rewritten in an orthorhombic lattice form with the basic lattice vectors of $\mathbf{a'_{C16}} = [110]_{C16} = \mathbf{a_{Cb}}/2$, $\mathbf{b'_{C16}} = [1\bar{1}0]_{C16} = \mathbf{b_{Cb}}$ and $\mathbf{c'_{C16}} = [001]_{C16} = \mathbf{c_{Cb}}$. Thereafter, the C16, C_b, N1 and the other polytypic structures can be finally written in a unified orthorhombic lattice form with basic lattice vectors of $\mathbf{a} = n^* \mathbf{a_{Cb}}/4$ (n represents the period number), $\mathbf{b} = \mathbf{b_{Cb}}$ and $\mathbf{c} = \mathbf{c_{Cb}}$. Importantly, considering the limitation of translational periodicity, the value of number $\mathbf{n}$ can only take some special integer, e.g. $\mathbf{n} = 2$ corresponding to C16 structure, $\mathbf{n} = 3$ corresponding to N1 structure, and $\mathbf{n} = 4$ corresponding to C_b structure. To some extent, polytypic M₂B-type borides can also be treated as a long period stacking order structure with variant periodic distances along the $[100]_{Cb}$ direction. Moreover, the specific stacking sequences can have many forms, even with the same period when $\mathbf{n}$ is bigger. In particular, to compare with the N1 structure, one of the $\mathbf{n} = 6$ polytypic structures (referred to as N2 indicated in the orthorhombic lattice form) projected along the $[001]_{N2}$ direction is given in Fig. 10c with the simplified description shown in Fig. 10d. It is meaning-
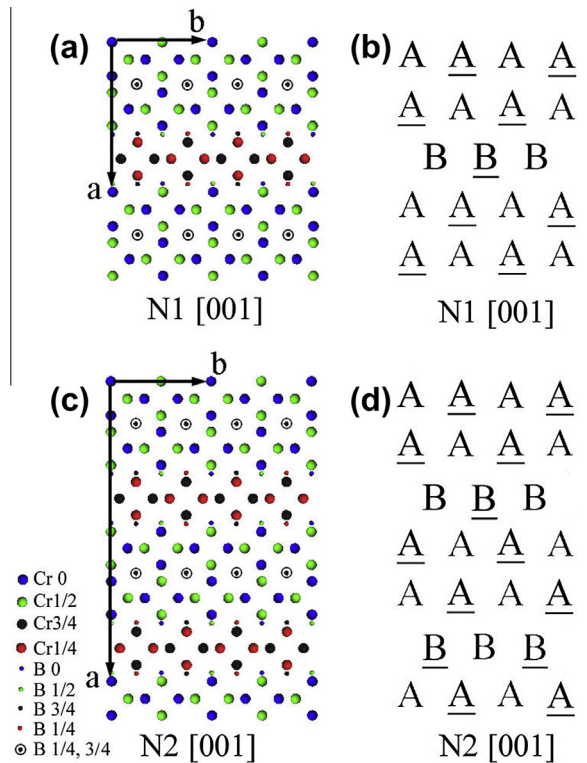

Fig. 10. Structure projection (a) and the corresponding simplified description (b) for N1 structure along the $[001]_{N1}$ direction; Structure projection (c) and the corresponding simplified description (d) for N2 structure along the $[001]_{N2}$ direction. The newly formed structures caused by ordered stacking of structure units A, $\underline{A}$, B, $\underline{B}$ are demonstrated. The atomic fractional coordinates and the lattice vectors of $\mathbf{a}$ and $\mathbf{b}$ are written in the orthorhombic form for both N1 and N2 structures.

ful to note that it is impossible to distinguish N1 and N2 structure along the $[001]$ zone-axis owing to the loss of height information along the projected directions in HRTEM mode.

3.3. Structural observation at an atomic scale

The nano-scaled intergrowth and structural similarity of M_2B-type borides results in complexity in resolving the various microstructures in these borides. For instance, the EDP of $[001]_{Cb}$ and $[010]_{Cb}$ zone-axes are the same as those of $[1\,1\,1]_{C16}$ and $[1\,\bar{1}\,3]_{C16}$ zone-axes. Similarly, the atomic projections from these directions are not helpful for distinguishing these structural variants. To avoid this problem, observations by tilting the sample to other zone-axes are necessary and, by doing so, some critical issues can be clarified at an atomic scale, such as displacement vectors of the stacking faults, 60° rotation twin, intergrowth of C16 and C_b structure as well as new ordered structures.

3.3.1. Stacking faults in C16 structure

To identify the displacement vector of stacking faults, HRTEM observations along different crystallographic directions are performed. Fig. 11a is a typical HRTEM image of faulted C16 structure viewed along the $[001]_{C16}$ direction, with stacking faults indicated by arrows. In the present observation, the stacking faults always penetrate through the whole M_2B grain. In Fig. 11a, the faulted plane for C16 structure is the $(1\,1\,0)_{C16}$ plane, and the displacement vector fraction is $[1\,\bar{1}\,0]_{C16}/4$ measured in the $[001]_{C16}$ projection. Fig. 11b shows another HRTEM image of faulted C16 structure viewing along the $[1\,\bar{1}\,0]_{C16}$ direction, which is perpendicular to $[001]_{C16}$. In Fig. 11b, the displacement vector fraction is $[001]_{C16}/4$. Therefore, one can determine the complete displacement vector of stacking faults to be $[1\,\bar{1}\,1]_{C16}/4$ for the C16 structure,

which agrees well with the crystallographic considerations in Section 3.2.3. The detailed atomic configurations for the stacking fault along the $[001]_{C16}$ direction are displayed in Fig. 9a.

3.3.2. 60° Rotation twin and stacking faults in C_b structure

Fig. 12a and b are HRTEM images obtained from the same area, but with different directions. Two areas (I and II) can be identified by boundaries, which are denoted by arrows. In Fig. 12a, area I is uniquely determined along the $[013]_{Cb}$ direction of C_b, but area II can be regarded either as the $[010]_{Cb}$ direction of C_b or as the $[1\,\bar{1}\,3]_{C16}$ direction of C16, since they correspond to the same EDP shown in Fig. 12d and e. To remove this ambiguity, Fig. 12b is then acquired by tilting the holder ~30° along the $[100]_{Cb}$ direction. Based on the determination of area II in Fig. 12b as the $[01\,\bar{1}]_{Cb}$ direction, area II in Fig. 12a can be determined unambiguously as the $[010]_{Cb}$ direction of C_b. By comparing Fig. 12a with b, it is found that, when area I is tilted from the $[013]_{Cb}$ to the $[011]_{Cb}$ direction about the $[100]_{Cb}$ normal direction, area II is tilted from the $[010]_{Cb}$ to the $[01\,\bar{1}]_{Cb}$ direction. Fig. 12f is a schematic illustration displaying the zone-axes alternation during the rotation along the $[100]_{Cb}$ direction for the C_b structure. Interestingly, the angles between $[013]_{Cb}$ and $[010]_{Cb}$, and $[011]_{Cb}$ and $[01\,\bar{1}]_{Cb}$ are all nearly 60° in the C_b structure. So area I and II should be treated as a 60° rotation twin relationship with the rotation axis along the $[100]_{Cb}$ direction, as speculated in Section 3.2.1.

Additionally, Fig. 12a contains a single stacking fault, indicated by the oblique lines representing the $(101)_{Cb}$ plane. It is seen that the faulted plane is $(100)_{Cb}$, and the displacement vector in the $[010]_{Cb}$ direction can be determined as $[001]_{Cb}/4$ for the C_b structure. To acquire the remaining segment vector, HRTEM images viewed along the $[001]_{Cb}$ direction of the C_b structure are given in Fig. 12c, with the stacking fault indicated by the arrow.
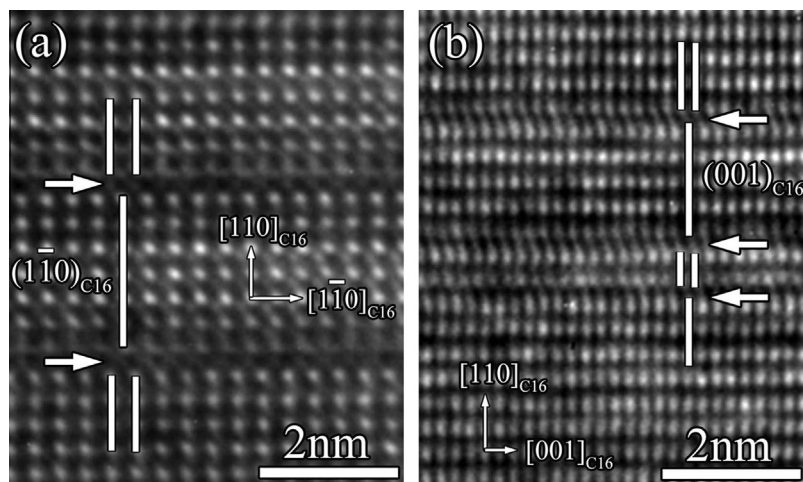

Fig. 11. (a) $[001]_{C16}$ and (b) $[1\,\bar{1}\,0]_{C16}$ HRTEM images of a C16 structure with stacking faults indicated by arrows. The vertical lines in (a) and (b) correspond to $(1\,\bar{1}\,0)_{C16}$ and $(001)_{C16}$ planes, respectively.
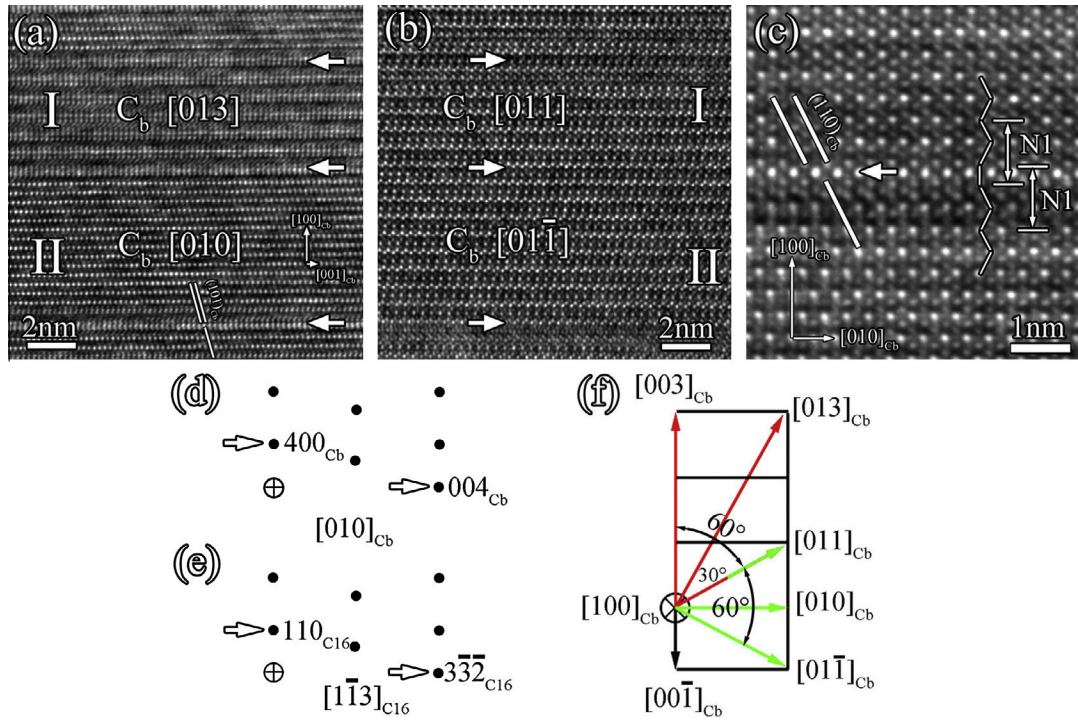
Fig. 12. (a) HRTEM image taken along the $[013]_{Cb}$ direction showing details of a 60° rotation twin in the C_b structure. The lower part of the image corresponds to its twin form. (b) $\langle 011 \rangle_{Cb}$ lattice image taken from the same area as in (a) but with a 30° tilting angle along the $[100]_{Cb}$ direction. (c) $[001]_{Cb}$ HRTEM image of C_b structure with stacking faults indicated by the arrow. The oblique lines in (a) and (c) correspond to $(101)_{Cb}$ and $(110)_{Cb}$ planes of C_b structure, respectively. (d)–(e) A quarter of the simulated diffraction pattern of $[010]_{Cb}$ and $[1\bar{1}3]_{C16}$ zone-axes. Transmitted spot is highlighted with a circled cross. (f) Schematic displaying the zone-axis alternation during tilting along the $[100]_{Cb}$ direction for C_b structure.

The displacement vector segment for the stacking fault is $[010]_{Cb}/4$ in the $[001]_{Cb}$ direction. So the complete displacement vector for the stacking fault in the C_b structure is $[011]_{Cb}/4$, which corresponds well to the crystallographic consideration in Section 3.2.3. It is of interest to note that the stacking fault results in a new ordered polytypic structure (referred as N1), which is seen from the alternation of the stacking sequence, as displayed in Fig. 12c. Detailed information on the atomic configuration of the stacking fault along the $[001]_{Cb}$ direction and the related N1 structure is shown in Fig. 9c.

3.3.3. Intergrowth of C16 and C_b structure

Fig. 13a and b shows HRTEM images taken from different parts of a single M_2B grain. Fig. 13a can be determined as being along the $[001]_{C16}$ direction of the C16 structure. But for Fig. 13b, the interpretation of the HRTEM is ambiguous. One cannot distinguish whether it is $[001]_{Cb}$ or $[1\bar{1}1]_{C16}$, because of the same distribution of EDP as shown in Fig. 13d and e. To differentiate the details, the holder is tilted about 30° along the $[110]_{C16}$ direction for the C16 structure. Then Fig. 13c is acquired from the same area as in Fig. 13b. Fig. 13c can be decided to be along the $[013]_{Cb}$ direction for the C_b structure unambiguously. So Fig. 13b should be determined along the $[001]_{Cb}$ direction of the C_b structure (see Fig. 12f for the zone-axes alternation). Now it is clear to see the intergrowth of C16 and C_b with the normal basic orientation relationships of

$[001]_{C16}//[001]_{Cb}$ and $(110)_{C16}//(100)_{Cb}$, which corresponds well to the crystallographic considerations in Section 3.2.2. During the experimental procedure, lattice images along both $[001]_{C16}$ and $[001]_{Cb}$ directions are always separated by many stacking faults in-between, which cannot fit well in one single image.

In addition, owing to the resolution limitation of the TEM, the skeleton of metal atoms for the structural units (A, $\underline{A}$, B and $\underline{B}$ in Fig. 7a and c) cannot be distinguished along the $[001]$ direction for both C16 and C_b structures. However, the stacking sequence for the structure units can be determined well in the HRTEM images. Corresponding to Fig. 7b and d, stacking sequences of the structural units for C16 and C_b structure along the $[001]$ direction are also identified and superposed on Fig. 13a and b, respectively.

Fig. 14 is a HRTEM image acquired from the heavily faulted area. The top part of the image corresponds to the projection of the C16 structure along the $[001]_{C16}$ direction. Stacking faults also appear in this region, as indicated by horizontal arrows. The bottom part of the image corresponds to the projection of C_b structure along the $[011]_{Cb}$ direction. Now the twin-related intergrowth mode with the orientation relationship of $[001]_{C16}//[011]_{Cb}$ and $(110)_{C16}//(100)_{Cb}$ can be determined, which corresponds well to the crystallographic considerations in Section 3.2.2. Moreover, the interface between C16 and C_b structures is coherent, and no misfit dislocation is found. Similarly,
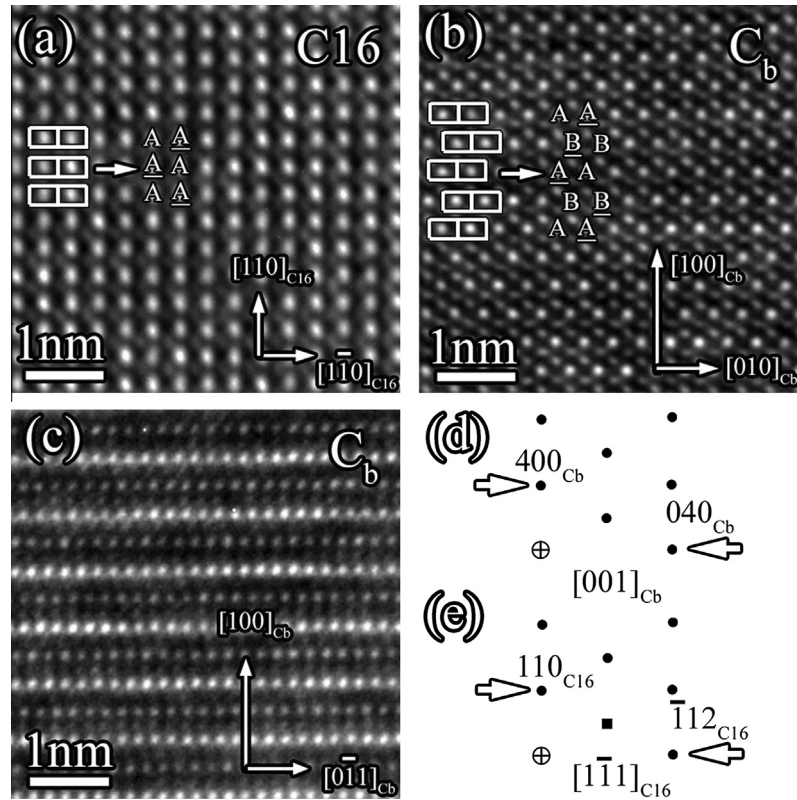
Fig. 13. HRTEM images obtained from different areas of one single grain with the same tilting angle corresponding to (a) $[001]_{C16}$ and (b) $[001]_{Cb}$ directions, showing the normal intergrowth of C16 and C_b structure. (c) $[013]_{Cb}$ lattice image taken from same the area as (b) but with 30° tilting angle along the $[110]_{C16}$ direction. The superposed letters (A, $\underline{A}$, B and $\underline{B}$) represent the stacking sequences of the structure units. (d)–(e) A quarter of the simulated diffraction pattern of $[001]_{Cb}$ and $[1\bar{1}1]_{C16}$ zone-axes. Transmitted spot is highlighted with a circled cross. The solid square represents double diffractions resulting from dynamic effects.
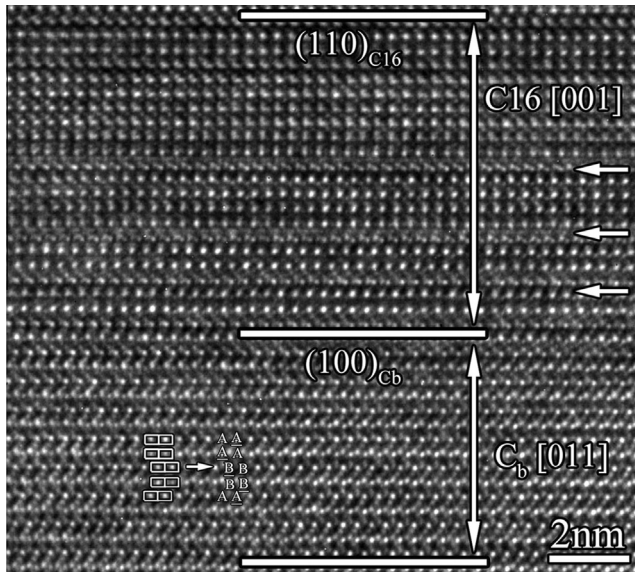

Fig. 14. HRTEM image showing the twin-related intergrowth of C16 and C_b structures. Stacking faults in C16 structure are denoted by arrows. The upper and lower parts of the image corresponds to $[001]_{C16}$ and $[011]_{Cb}$ direction, respectively.

corresponding to Fig. 8d, stacking sequences of the structural units for C_b structure along the $[011]_{Cb}$ direction are also superposed on the bottom part of Fig. 14.

3.3.4. Other new polytypic structures

M_2B grain is full of stacking faults as seen in Fig. 1. It is proposed that any periodic array of stacking faults can result in new polytypic structures. Based on the unified orthorhombic lattice form for various polytypic structures, the parameters for polytypism can be expressed as $a = (0.37n)$ nm (n = some integer; for C16, $n = 2$; for N1, $n = 3$; for C_b, $n = 4$), $b = 0.74$ nm and $c = 0.43$ nm. So the specified structure can be distinguished based on the different periods along the $[100]_{Cb}$ direction. Here, the basic spacing distance d (0.37 nm) is introduced into the polytypic analysis. In Fig. 15a, the HRTEM image displays the intergrowth of the $3d$ and $4d$ period viewed along the $[011]_{Cb}$ direction. It is known that the $4d$ period corresponds to the C_b structure. As for the $3d$ period, it can correspond to the N1 structure. Moreover, its true period could also be $6d$. Then, the $3d$ period only corresponds to the sub-cell of N2 structure. Detailed information for the N1 and N2 structure is shown in Fig. 10a–d. Fig. 15b is an HRTEM image displaying a nano-scale ordered structure with $3d$ or $6d$ period in M_2B viewed along the $[011]_{Cb}$ direction. If deemed to be N1 structure with $3d$ period, corresponding to Fig. 10b, the stacking sequence of the structural units along the $[001]_{N1}$ direction is superposed on the top right-hand side of Fig. 15b. However, if deemed to be N2 structure with $6d$ period, corresponding
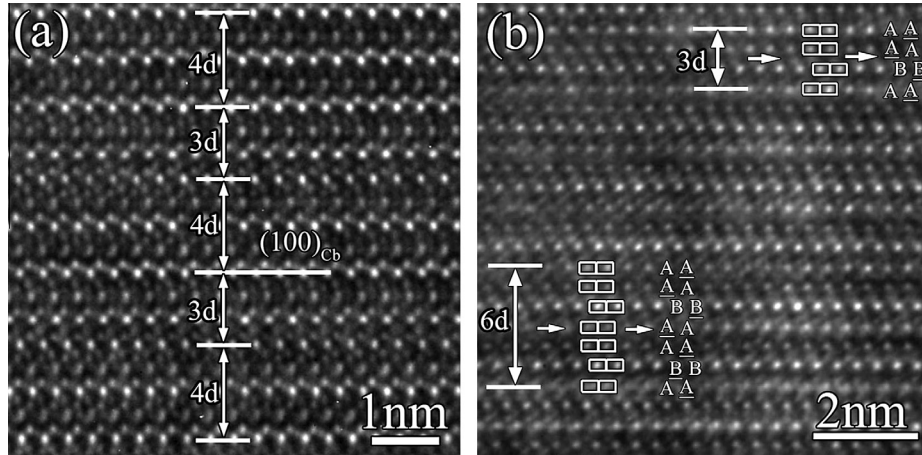
Fig. 15. (a) HRTEM image viewed along $[011]_{Cb}$ showing the intergrowth of various structures with different periodicities stacking along the $[100]_{Cb}$ direction. The basic distance d equals 0.37 nm. (b) Repeated stacking faults in (100) plane resulting in new local structure with periodicity of $3d$ or $6d$.

to Fig. 10d, the stacking sequence of the structural units along the $[001]_{N2}$ direction is superposed on the bottom left-hand side of Fig. 15b.

4. Conclusions

Based on microstructural investigations, the crystallography of the nano-scaled intergrowth of M_2B-type borides in nickel-based superalloys has been discussed. The following conclusions can be drawn:

1. The M_2B-type precipitations in nickel-based superalloys containing boron subjected to long-term aging treatments display a number of structural variants. Some M_2B precipitates can be well identified C16 or C_b structure, while some precipitates possess dual-phase characteristics with highly dense stacking faults.
2. The atomic planes and displacement vectors of stacking faults are determined as $(110)_{C16}$, $[1\bar{1}1]_{C16}/4$ in C16 structure and $(100)_{Cb}$, $[011]_{Cb}/4$ in C_b structure.
3. In both C16 and C_b structures, 60° rotation twins are identified with rotation axes along the $[110]_{C16}$ and $[100]_{Cb}$ direction, respectively. And the detailed parallel relationships for the rotation twin can be specified as $[002]_{C16}//[1\bar{1}1]_{C16-T}$, $[2\bar{2}0]_{C16}//[1\bar{1}3]_{C16-T}$, $[110]_{C16}//[110]_{C16-T}$ in C16 structure and $[002]_{Cb}//[011]_{Cb-T}$, $[020]_{Cb}//[01\bar{3}]_{Cb-T}$, $[100]_{Cb}//[100]_{Cb-T}$ in C_b structure.
4. Two intergrowth modes are distinguished in the C16 and C_b structure. For the basic mode, the orientation relationship is derived as $[001]_{C16}//[001]_{Cb}$, $[1\bar{1}0]_{C16}//[010]_{Cb}$ and $[2\bar{2}0]_{C16}//[100]_{Cb}$. While for the twin-related intergrowth mode, the parallel relationship is determined as $[002]_{C16}//[011]_{Cb}$, $[2\bar{2}0]_{C16}//[01\bar{3}]_{Cb}$, $[2\bar{2}0]_{C16}//[100]_{Cb}$ or $[1\bar{1}1]_{C16}//[002]_{Cb}$, $[1\bar{1}3]_{C16}//[020]_{Cb}$, $[2\bar{2}0]_{C16}//[100]_{Cb}$.
5. The crystal structure of the M_2B-type borides can be outlined in terms of polytypism, whose representative characteristic is the conservation of the basic square anti-prism building block which consists of one boron atom in the center and eight metal atoms in the vertex. A unified orthorhombic lattice form is proposed to describe the lattice vector for different structural variants, namely $\boldsymbol{a} = n^* \boldsymbol{a_{Cb}}/4$ ($n = 2$ for C16; $n = 3$ for N1; $n = 4$ for C_b), $\boldsymbol{b} = \boldsymbol{b_{Cb}}$ and $\boldsymbol{c} = \boldsymbol{c_{Cb}}$.

References

[1] Perepezko JH. Science 2009;326:1068.
[2] Reed RC. The Superalloys: Fundamentals and Applications. Cambridge: Cambridge University Press; 2006.
[3] Holt RT, Wallace W. Int Metals Rev 1976;21:1.
[4] Floreen S, Davidson JM. Metall Trans A 1983;14:895.
[5] Zhou PJ et al. Mater Sci Eng A 2008;491:159.
[6] Ojo OA, Zhang HR. Metall Mater Trans A 2008;39:2799.
[7] Zhang HR et al. Scripta Mater 2008;58:167.
[8] Zhang HR, Ojo OA. J Mater Sci 2008;43:6024.
[9] Zhang HR, Ojo OA. Philos Mag 2010;90:765.
[10] Thuvander M, Stiller K. Mater Sci Eng A 2000;281:96.
[11] Kaufman MJ, Levit VI. Philos Mag Lett 2008;88:259.
[12] García-Bórquez A, Kesternich W. Scripta Metall 1985;19:57.
[13] Goldfarb I et al. Philos Mag A 1995;72:963.
[14] Kayser FX, Kayser GF. J Mater Sci 1999;34:1271.
[15] Sourmail T et al. Scripta Mater 2004;50:1271.
[16] Mansfield JF. Convergent Beam Electron Diffraction of Alloy Phases. Bristol: Alden Press; 1984.
[17] Kilaas RJ. Microscopy 1998;190:45.
[18] Frank FC, Kasper JS. Acta Crystallogr 1958;11:184.
[19] Frank FC, Kasper JS. Acta Crystallogr 1959;12:483.
[20] Dudzinski W et al. J Mater Sci 1980;15:1387.
[21] Morniroli JP et al. Philos Mag A 1983;48:311.
[22] Morniroli JP et al. Philos Mag A 1987;56:93.
[23] DeGraef M et al. Acta Metall Mater 1991;39:2381.
[24] DeGraef M et al. Acta Metall Mater 1992;40:3395.